Sedimentary response to current and nutrient regime rearrangement in the Eastern Mediterranean Realm during the early to middle Miocene (southwestern Cyprus)

Bialik, O.M.*[1,2,3], Reolid, J.[4], Kulhanek, D.K.[5,6], Hincke, C.[1], Waldmann, N.D.[2] & Betzler, C.[1]

1. Institute of Geology, CEN, University of Hamburg, Bundesstrasse 55, Hamburg 20146, Germany.

2. Dr. Moses Strauss Department of Marine Geosciences, The Leon H. Charney School of Marine Sciences, University of Haifa, Carmel 31905, Israel.

3. Marine Geology & Seafloor Surveying, Department of Geosciences, University of Malta, Msida, Malta. (Current address)

4. Departamento de Estratigrafía y Paleontología, Universidad de Granada. Avenida de la Fuente Nueve SN, 18071, Granada, Spain.

5. International Ocean Discovery Program, Texas A&M University, 1000 Discovery Drive, College 10 Station, TX77845, USA

6. Institute of Geosciences, University of Kiel, D-24118 Kiel, Germany. (Current address)

This paper is a non-peer review preprint submitted to EarthArXiv, which has been submitted to Palaeogeography, Palaeoclimatology, Palaeoecology for peer review.

Sedimentary response to current and nutrient regime rearrangement in the Eastern Mediterranean Realm during the early to middle Miocene (southwestern Cyprus)

Bialik, O.M.*[1,2,3], Reolid, J.[4], Kulhanek, D.K.[5,6], Hincke, C.[1], Waldmann, N.D.[2] & Betzler, C.[1]

1. Institute of Geology, CEN, University of Hamburg, Bundesstrasse 55, Hamburg 20146, Germany.

2. Dr. Moses Strauss Department of Marine Geosciences, The Leon H. Charney School of Marine Sciences, University of Haifa, Carmel 31905, Israel.

3. Marine Geology & Seafloor Surveying, Department of Geosciences, University of Malta, Msida, Malta. (Current address)

4. Departamento de Estratigrafía y Paleontología, Universidad de Granada. Avenida de la Fuente Nueve SN, 18071, Granada, Spain.5. International Ocean Discovery Program, Texas A&M University, College Station, TX 77845, USA.

5. International Ocean Discovery Program, Texas A&M University, 1000 Discovery Drive, College 10 Station, TX77845, USA

6. Institute of Geosciences, University of Kiel, D-24118 Kiel, Germany. (Current address)

*Corresponding author (orbialik@campus.haifa.ac.il)

Abstract

During the early and middle Miocene, the Mediterranean had become a restricted marginal marine sea with diminishing and ultimate loss of connectivity to the Indian Ocean. This dramatically changed the heat, energy, freshwater and nutrient budgets across the Mediterranean and most notably in its eastern basin. While one of the most prominent lines of evidence of this change in the Eastern Mediterranean is the onset of sapropel formation, many other aspects of the sedimentary system changed in response to this rearrangement. Here we present a detailed analysis of a hemipelagic succession from southeastern Cyprus dated to the late Aquitanian to the early Serravallian (22.5 – 14.5 Ma). This sequence is carbonate-dominated and formed during the decoupling of the Mediterranean Sea and the Indian Ocean. It exhibits sedimentation with mass transport contribution from shallow water carbonates to deeper facies with phosphatization and bottom current (at intermediate depth) interactions. This succession traces both local subsidence and loss of a local carbonate factory. Additionally, it records a shift in bottom current energy and seafloor ventilation, which are an expected outcome of connectivity loss with the Indian Ocean.

Keywords: Pakhna formation, Drift deposits, Pelagite, Sapropels, Phosphogenesis

Introduction

The Miocene evolution of the Mediterranean realm witnessed significant shifts in climatic and ocean circulation patterns. This shift was part of a global driven by global cooling, enhanced glaciation of Antarctica and rearrangement of the worldwide current regime rearrangement (Betzler et al., 2016; Betzler and Eberli, 2019; Flower and Kennett, 1994; Groeneveld et al., 2017; Hamon et al., 2013; Miller et al., 1991; Pound et al., 2012). In the Mediterranean Sea these forcings were amplified by tectonics, which decoupled it's water mass from the Indian Ocean in the early and middle Miocene (Bialik et al., 2019; Reuter et al., 2013; Rögl et al., 1998), from the Paratethys in the middle to late Miocene (Flecker and Ellam, 2006; Sant et al., 2017; Simon et al., 2018) and from the Atlantic Ocean in the late Miocene (Flecker et al., 2015; Meilijson et al., 2019; Seidenkrantz et al., 2000).

The combination of gateway evolution and climate shifts resulted in modification of both the freshwater and nutrient budgets of the Mediterranean Sea, as well as the circulation pattern throughout the water column. The climate shift was marked by the transition from an arid to a humid climate in the late early Miocene (John et al., 2003), expansion of Saharan fluvial systems during the middle Miocene (Swezey, 2009) and extreme humidity in the late Miocene (Böhme et al., 2008), followed by extreme aridity in the latest Miocene (Griffin, 2002). The relative size of the Mediterranean Sea and the position of the intertropical convergence zone (ITCZ) were ascribed to be the principal drivers of these shifts with the Atlantic meridional overturning circulation (AMOC) having a contributing effect (Zhang et al., 2014). The changes in currents and climate in the Mediterranean fundamentally shifted the way it functioned. Through the Miocene fundamental shifts in phosphogenesis patterns (Auer et al., 2016; Föllmi et al., 2015), sedimentation patterns (Torfstein and Steinberg, 2020) and structure of shallow-water calcifying communities (Bosellini and Perrin, 2008; Pomar and Hallock, 2007) occurred. Modelling work suggests that the direct effects of the change in connectivity were the reversal of zonal circulation in the upper water column and reduced turnover of the lower water column (de la Vara, 2015; de la Vara et al., 2013; de la Vara and Meijer, 2016), which might have reduced ventilation. This shift also led to the rise of the modern Mediterranean Sea circulation. This circulation is marked by high turnover and rapid generation of intermittent water mass (Robinson et al., 1992), oligotrophic to extreme oligotrophic state (Magazzù and Decembrini, 1995; Reich et al., 2021) and strong sensitivity to fresh water input – which may generate sapropel events (Blanchet et al., 2021; Zirks et al., 2021, 2019). The latter is consistent with the initiation of sapropel deposition (Rohling et al., 2015; Taylforth et al., 2014) occurring towards the end of the transition period from open to closed connectivity with the Indian Ocean (Bialik et al., 2019).

Here we investigate the response of hemipelagic carbonate-dominated depositional patterns to these rearrangements during the early and middle Miocene in the eastern Mediterranean (Figure 1a). This area was radically altered from being connected directly to the global oceans into a marginal marine setting mostly isolated from the global oceans during this period. In addition, this area includes the oldest known sapropels from the Mediterranean Basin (Athanasiou et al., 2021; Shipboard Scientific Party, 1978; Taylforth et al., 2014). This study presents a complete continuous section dated to the Aquitanian to the Langhian using nannofossil biostratigraphy from southern Cyprus. Detailed facies analysis of this section, deposited on a southern slope, records notable sea-level fluctuations and changes in the nutrient and current regimes.

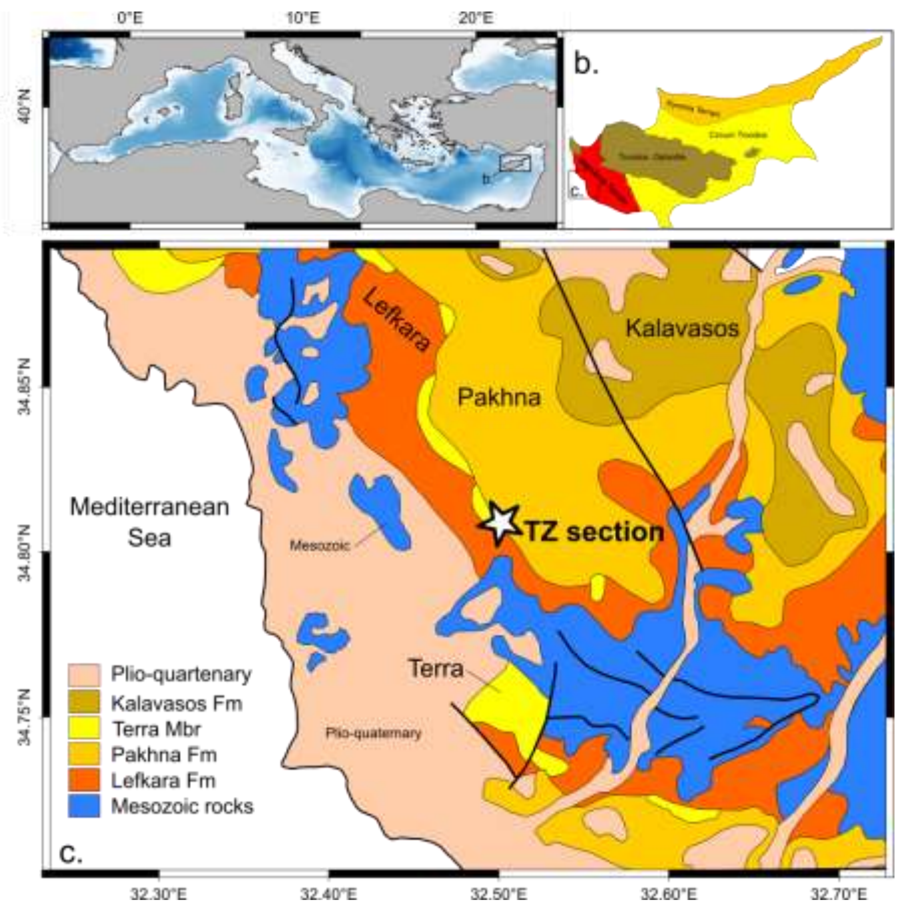

Figure 1: Location maps. a. Map of the Mediterranean showing the location of Cyprus. b. Main geological domains in Cyprus (Robertson, 1977). c. Geological map of the general study area (Geological survey department, 1979) and the location of the TZ section near Tsada.

Geological setting

The early and middle Miocene in southern Cyprus is represented by the upper part of the Lefkara Formation (upper marl member) and the Pakhna Formation (Eaton and Robertson, 1993; Kähler and Stow, 1998; Robertson, 1976). Both were dominantly deposited in a deeper water environment and are comprised of hemipelagic to pelagic marls and chalks with beds of redeposited coarser calcareous material (described as calcarenite and calcirudite). Inconsistencies exist in the lithological description and assignment of the Oligocene-Miocene lithostratigraphy of southern Cyprus, partially owing to significant lateral gradients (Eaton and Robertson, 1993). Synthesizing the available sources (Bagnall, 1960; Hüneke et al., 2021; Kähler and Stow, 1998; Papadimitriou et al., 2018; Robertson, 1976; Robertson and Hudson, 2009) the upper part of the Lefkara Formation consists of pale to white calcareous material (marl to chalk), ranging from mudstone to packstone in texture, locally with coarse reworked material. The lower part of the Pakhna Fm is pale to white calcareous material ranging from mudstone to packstone, with local floatstone to rudstone. The character of the rock is more competent than the upper Lefkara Fm and includes limestone horizons. HIgher up in the Pakhna Fm, the character shifts back to more fine-grained marly deposits. These have been described in most detail in the outcrops of Petra Tou Romiou (Hüneke et al., 2021; Miguez-Salas and Rodríguez-Tovar, 2019; Rodríguez-Tovar et al., 2019).The presence of calcarenite in the Lefkara and lower Pakhna formations, notably in the upper Oligocene and lower Miocene, was attributed to contourites (Kähler and Stow, 1998; Stow et al., 2002). Multiple types of contourite deposits were inferred in southwest Cyprus, all related to slope environments, intermixed with turbidites and perturbated by bioturbation (Hüneke et al., 2021). This bioturbation in some places might be mistaken for sediment structures generated by bottom currents (Reolid et al., 2020). In a few locations on the Mamonia Terrain (Figure 1b), as well as on the southeastern edge of the island, shallow water lower Miocene deposits are present and mapped as the Terra member of the Pakhna Formation (Follows, 1992). On the Mamonia Terrain, the formation of these shallow water regions was attributed to local highs which formed atop large thrust faults related to uplift of the Troodos Massif and the continued collision of Cyprus and the Eratosthenes block to the south (Follows et al., 1996; Papadimitriou et al., 2018). However, the specific mechanism is debated, with some arguing for a horst and graben structure (Balmer et al., 2019; Cannings et al., 2021), whereas others call for blind thrusts (Papadimitriou et al., 2018) to generate the highs the reefs developed on. The former would result in steep slopes while the latter in gentler slopes with piggyback basins.

At the same time, the area north of the Troodos Massif (Mesaoria Basin and Kyrenia Range) was also located in a deep water environment, receiving sediment supply from the Anatolia and Taurides regions (Shaanan et al., 2021). In this environment sediment exhibiting intermittent oxygen stress began to appear during the Langhian, at ca. 15.5 Ma (Athanasiou et al., 2021; Taylforth et al., 2014); these have been suggested to be early sapropels or precursors of the sapropels. These layers appear to be generated in a warm but dominantly oligotrophoic setting, under eccentricity and obliquity modulation (Athanasiou et al., 2021) rather than the precessional forcing characterizing later saproples (Kroon et al., 2004; Larrasoaña et al., 2003; Rohling et al., 2015).

Methods

Samples were collected on the outskirts of the village of Tsada, Cyprus (34.8295°N, 32.4748°E, Figure 1c). A composite section (TZ) was measured along road outcrops in a residential area. The area was mapped to control and correct for displacement due to local faulting. Ninety eight samples were collected along the section as allowed by exposure and accessibility conditions. Thin sections were prepared from all collected samples following resin impregnation with blue dye. Thin sections were described using a petrographic microscope. Texture classification was done in accordance with the Dunham (1962) classification, relative abundances of all allochems were semiquantitavely assessed for each sample (ranked abundant, common, several, rare and present). Additional photomicrographs are included in Supplement 1. Carbonate content was measured using a LECO device at the University of Hamburg. Stable isotopes analysis was carried out using bulk rock samples. Dried samples were crushed, weighted, reacted with H_3PO_4 under He atmosphere. Discharged CO_2 was measured for carbon and oxygen isotope composition using a Finnigan MAT 251 equipped with a Carbo-Kiel Device (Type I) at the Leibniz-Labor für Altersbestimmung und Isotopenforschung at the University of Kiel. All values are reported as permil (‰) relative to Vienna PeeDee belemnite (VPDB). Isotope and carbonate content values are reported in Supplement 2.

Biostratigraphy

Samples for calcareous nannofossil examination were prepared using the standard smear slide technique (Bown and Young, 1998). A small amount of sediment was scraped onto a coverslip from a fresh surface of a rock chip using a razor blade. A drop of deionized water buffered with ammonium hydroxide to pH 8.5 was added to the coverslip and mixed with the sediment using a round toothpick to form a slurry, which was then spread evenly over the coverslip and dried on a hot plate. The coverslip was affixed to a glass microscope slide using Norland Optical Adhesive No. 61 and cured under ultraviolet light for a minimum of 10 minutes. Samples were examined at up to 1250× using a Zeiss Axioscope 5 transmitted light microscope under cross-polarized, plane-transmitted, and phase contrast light. A minimum of 400 fields of view were scanned on each slide for biostratigraphically useful taxa to develop a biostratigraphic framework for the studied section. Taxonomic concepts for species are those given in Perch-Nielsen (1985), Bown (1998) and the Nannotax online catalogue (Young et al., 2019). Samples are assigned to the NN nannofossil zones of Martini, 1971 and CNM zones of Backman et al. (2012), with ages for bio-events assigned following Backman *et al.* (2012). Height of zone boundaries were assigned based on the mid-point between samples.

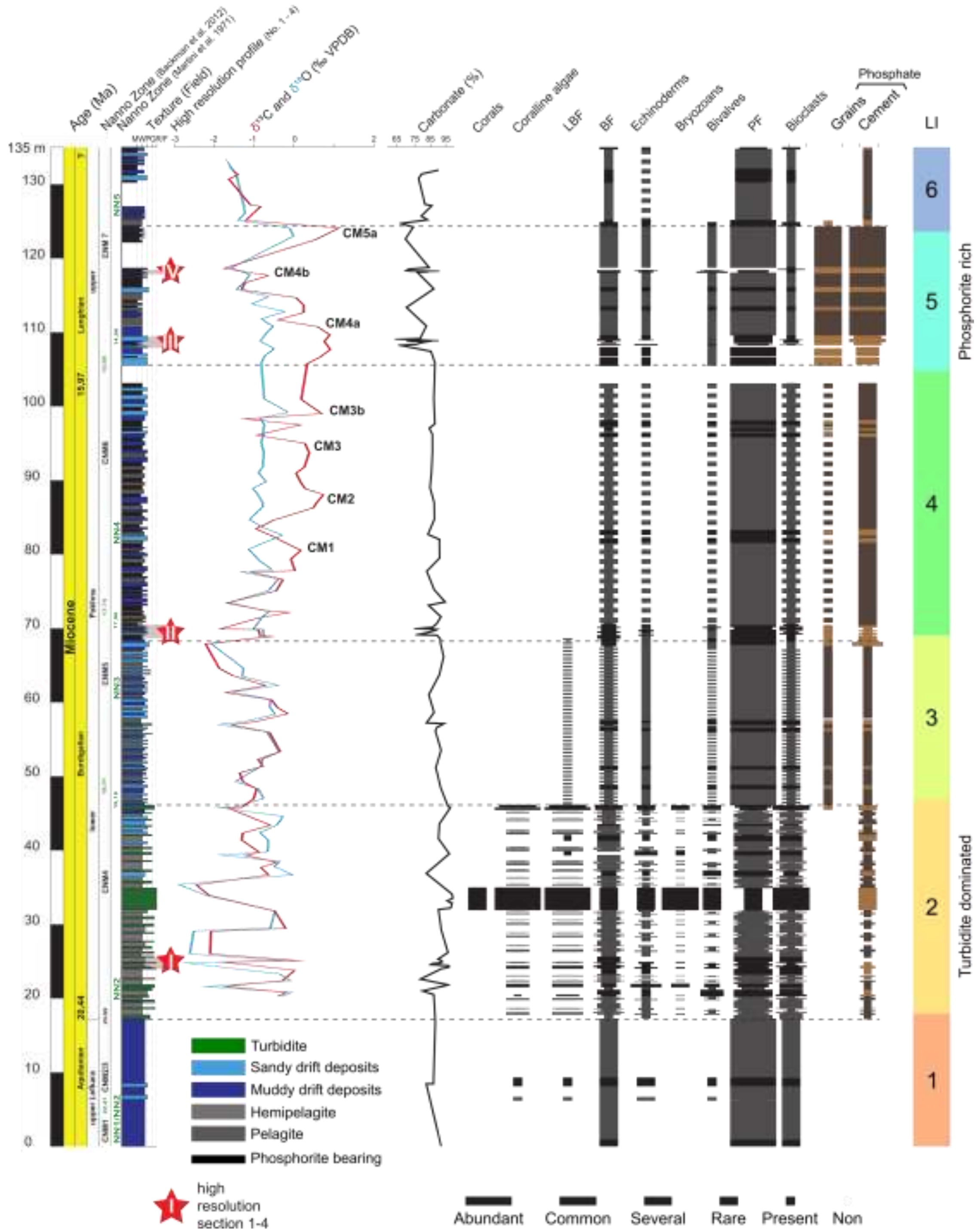

Figure 2: Composite stratigraphic column of the TZ section showing height in meters, age, nannofossil zones, lithology, texture, stable isotopes, carbonate weight percent, and allochems. CM = ^{13}C maxima, LBF = large benthic foraminifera, BF = benthic foraminifera, PF = planktonic foraminifera, LI = lithologic interval.

Results

Sedimentary succession

The TZ section consists of alternating beds of limestone, marl, and marly limestone. Mean carbonate content throughout the section is ~90%, and nearly 100% in the limestone beds (Fig. 2). The texture of the carbonates varies from mudstone to rudstone/floatstone. We delineated six lithological intervals (LI) in the section based on lithology and fossil content (Figure 2).

Lithological intervals 1 (0 to 18m) consists of marly limestone and minor limestone intervals and corresponds to the upper part of the Lefkara Fm. Deposits primarily are wackestone with common to abundant planktonic foraminifera as well as rare benthic foraminifera and unidentified bioclasts. In the limestone beds larger benthic foraminifera (LBF) and coralline algae are also found. Mean carbonate content in this interval is 87±3% (n=5). This unit hosts multiple horizons of "lenticular bedding" generated by *Zoophycos* burrows. More detailed analysis of the *Zoophycos* horizons and this part of the section can be found in Reolid *et al.* (2020).

Lithological intervals 2 (18 to 47m) is attributed to the lower part of the Pakhna Formation. It consists of an alternation of limestone and marly limestone (Figure 3a). The limestone beds are packstone to float/rudstone with soft sediment deformation. In places, coarse-grained intervals laterally wedge out (Fig. 4a). These beds can also reach several meters in thickness (Figure 4b). The limestone beds exhibit a vertical gradient both in grain size and composition, being finer in the upper part with only planktonic foraminifera and bioclasts (Figure 3b) to a coarser base with LBF (Figure 3c), coralline algae, some bryozoans and rare corals that can appear as sand size fragments to boulders (Figure 4c). The LBF include *Amphistegina*, *Operculina*, *Heterostegina*, *Lepidocyclina,* and *Miogypsina* as well as encrusting forms in some samples. The LBF are often abraded and fragmented. The marly limestone beds are mudstone to wackestone with mostly planktonic foraminifera. Bivalves and echinoderms as well as rare phosphatic cements appear in this interval and are present to the top of the section. $\delta^{13}C$ values in this interval range between -2.5‰ and 0.1‰ and exhibit shifts on the order of 2‰ between beds with lower values occurring primarily in limestone beds. Mean carbonate content in this interval is 93±6% (n=34) with higher values (up to 99%) in the limestone beds.

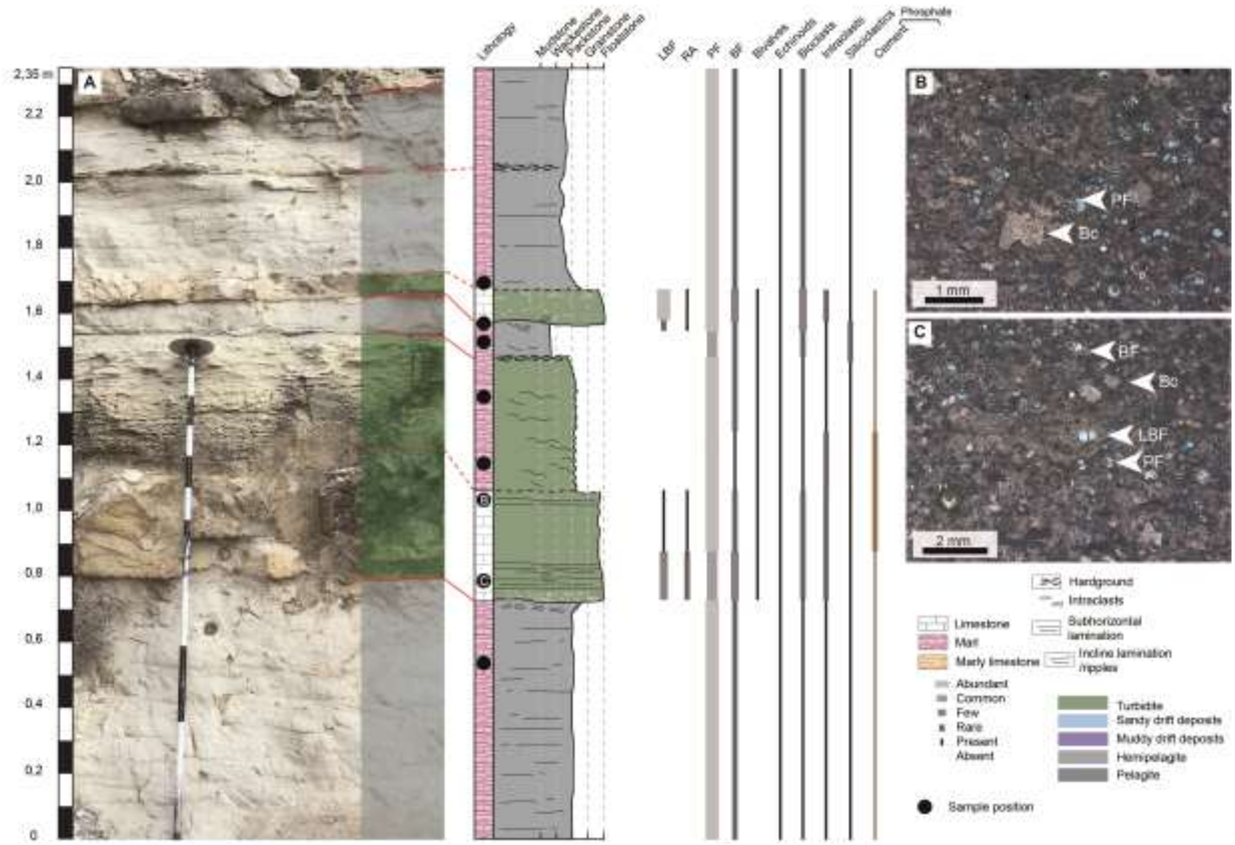

Figure 3: Representative section from LI2 (location denoted as I in Figure 2) showing (a) alternations between the more laminated marly pelagite facies and limestone mass transport deposits (MTD) facies. Photomicrographs (locations noted on lithological section) show the material transported and integrated into the MTDs, including more distal (b) reworked bioclasts (Bc) and planktonic foraminifera (PF) or more proximal (c) larger and smaller benthic foraminifera (LBF and BF, respectively). RA stands for coralline red algae.

Lithological intervals 3 (47 to 69m) is composed of alternating limestone and marly limestone. The couplets have a relatively consistent thickness of around 60 cm. The limestone beds are packstone to grainstone with benthic and planktonic foraminifera, including LBF; small bivalves and echinoderm fragments are also present. The marly limestone are wackestone with primarily planktonic foraminifera. Rare phosphatic grains and cements are encountered in all facies. $\delta^{13}C$ values in this interval range between -2.2‰ and -0.2‰ with lower values encountered in limestone beds and towards the top of the interval. Mean carbonate content in this interval is 90±3% (n=14).

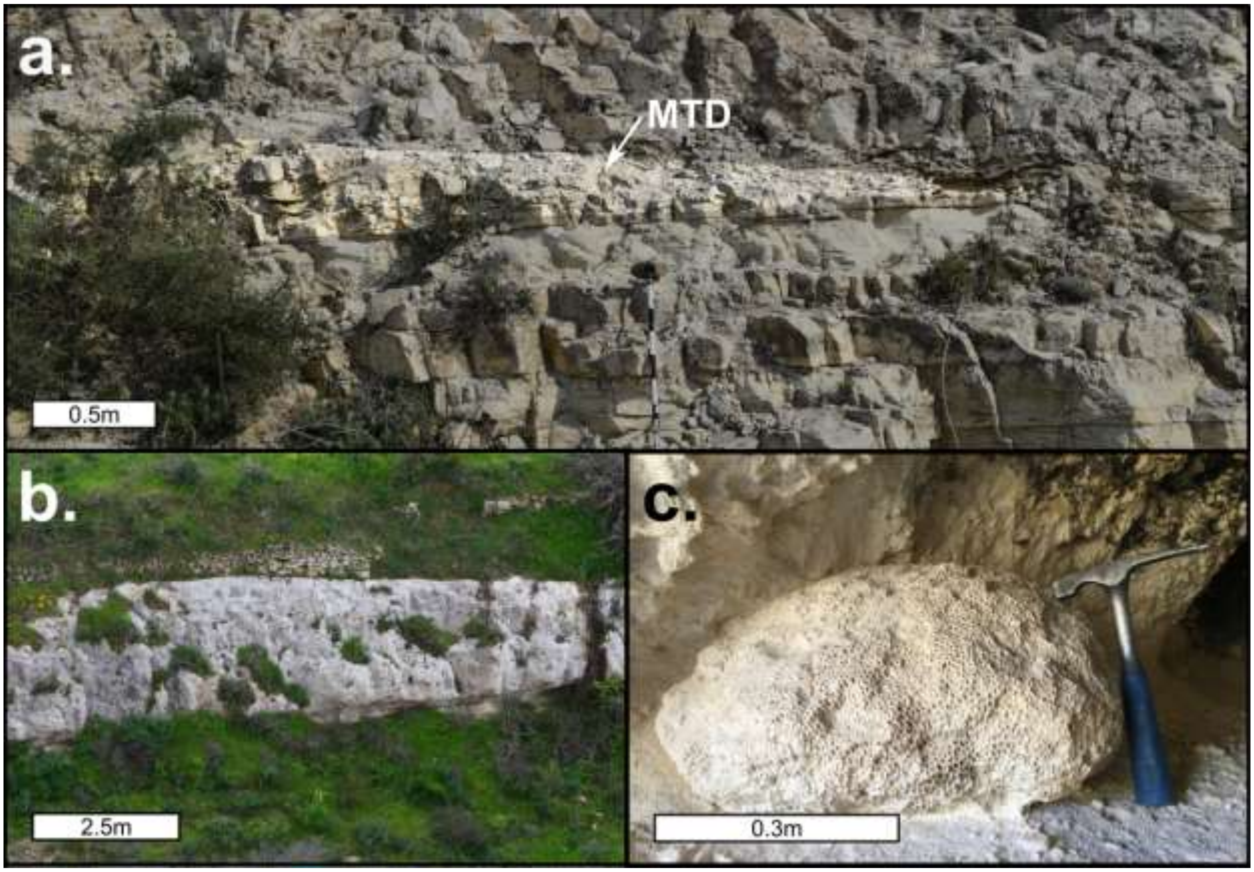

Figure 4: Sedimentary features in the TZ section. a. Mass transport deposits (MTD) in the lower part of the section (highlighted). b. Possible clinoforms within reworked beds. c. Corals within a large MTD.

Lithological intervals 4 (69 to 105m) consists of alternating limestone, marly limestone and marl (Figure 5a). Bed thickness is more irregular in this interval and varies between 10 and 80 cm. All lithologies range between wackestone and packstone and contain primarily planktonic foraminifera (Figure 5b-c), as well as benthic foraminifera and small amounts of unidentified bioclasts. Some beds include small bivalves and echinoderm fragments. Larger intraclasts may be present in the limestone beds, which may also exhibit irregular contacts. Phosphate cements are common, and phosphate grains are rarely encountered (Figure 5b). $\delta^{13}C$ values in this interval range between -1.9‰ and 0.8‰. Mean carbonate content in this interval is 87±4% (n=27).

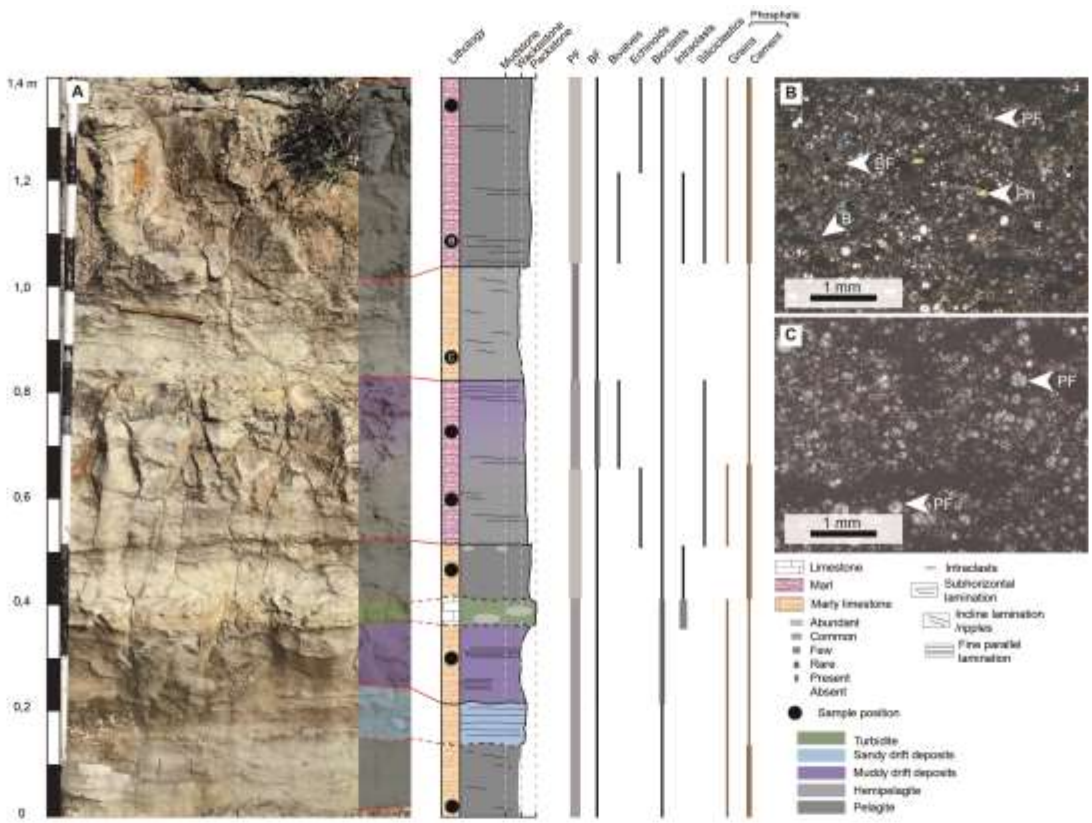

Figure 5: Representative section from LI4 (location denoted as II in Figure 2) showing (a) alternations between the more laminated marly hemipelagite to pelagite facies, grain rich drift facies and limestone mass transport deposits (MTD) facies. Photomicrographs (locations noted on lithological section) show the pelagite facies (b) and hemipelagite facies (c) with small thin walled bivalves (B), benthic and planktonic foraminifera (BF and PF, respectively) and phosphatic fragments (Ph).

Lithological intervals 5 (105 to 124m) consists mostly of an alternation between marly limestone and marl (Figure 6a) with few limestone beds (Figure 7a). The various lithologic beds range from 10 to 100 cm in thickness. The texture in this interval ranges from wackestone to packstone (densely packed at some horizons, Figure 6b), with abundant planktonic and few benthic foraminifera (Figure 6c); echinoderms, bivalves and bioclasts are present in most samples. Phosphatic grains and cement abundance increases significantly relative to underlying intervals (Figure 7b-d). Distinct bioturbation is present in a few beds (Figure 7b). $\delta^{13}C$ values in this interval range between -1.8‰ and 0.9‰. Mean carbonate content in this interval decreases to 78±7% (n=26). The higher variability in carbonate content does not correlation to the carbon isotopes where both analyses were done (r=-0.4, n=6).

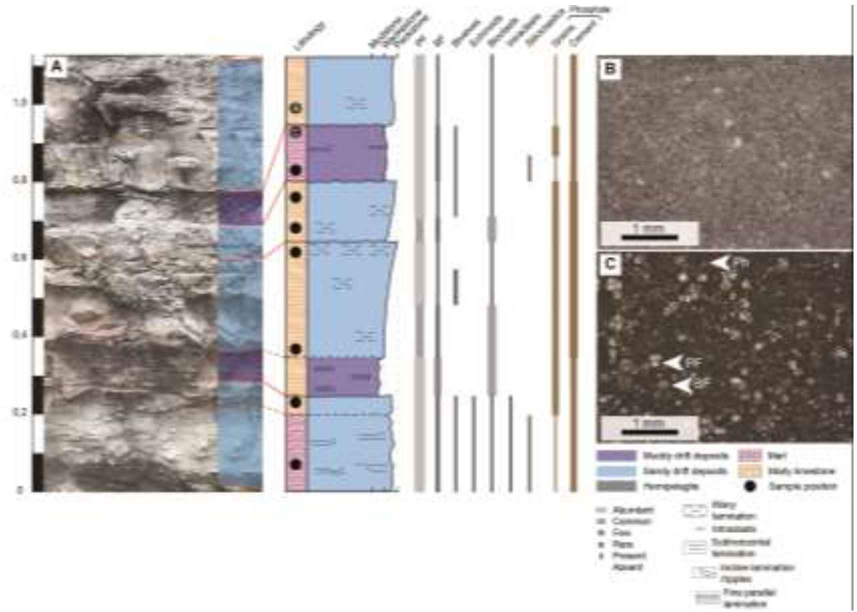

Figure 6: Representative section from LI5 (location denoted as III in Figure 2) showing (a) alternations between muddy and sandy drift facies. Photomicrographs (locations noted on lithological section) show the sandy drift facies (b) and muddy drift facies (c) with benthic and planktonic foraminifera (BF and PF, respectively) and phosphatic fragments (Ph).

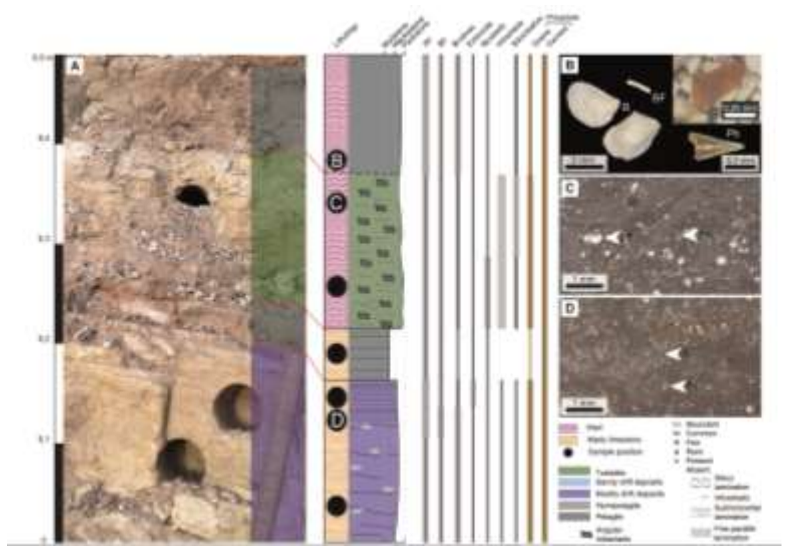

Figure 7: Representative section from LI5 (location denoted as IV in Figure 2) showing (a) alternations between the more laminated marly pelagite facies, muddy drift facies and limestone mass transport deposits (MTD) facies. Photomicrographs (locations noted on lithological section) show (b) washed small thin-walled bivalve (B), uniserial benthic foraminifera (BF) and fish tooth as well unrecognizable phosphatic fragments (Ph) from the pelagite facies, the muddy drift facies (c) and MTD facies (d) with bioturbation (BT) small thin-walled bivalves (B) and planktonic foraminifera (PF).

The topmost interval, LI6 (124m to 135m), consists of alternating marly limestones and marls. Both lithologies host primarily planktonic foraminifera and few benthic foraminifera, echinoderms, and unidentifiable bioclasts. Phosphate grains are not present, although phosphate cements are. $\delta^{13}C$ values in this interval range between -1.6‰ and 1.2‰. Mean carbonate content in this interval decreases to 80±7% (n=9) and appears to be increasing at the top of the studied section.

Age model and sedimentation rate

Nannofossil biostratigraphy

All samples contain common to abundant calcareous nannofossils. Preservation is variable throughout the section, although in general is moderate, with some samples better preserved than others. The assemblage is dominated by reticulofenestrids, and *Coccolithus pelagicus* and *C. miopelagicus* are also present throughout the studied interval. Pentaliths (including *Braarudosphaera* and *Micrantholithus*) are relatively common in a few samples. Additionally, the abundance of *Helicosphaera* and *Pontosphaera* vary significantly throughout the section. Reworked Cretaceous and Paleogene taxa are most common below 25 m, although rare specimens occur to the top of the section.

The lowest sample examined (1.94 m) is assigned to Zone CNM1 (Backman et al., 2012) based on the absence of both *Sphenolithus delphix* (last occurrence [LO] at 23.06 Ma) and *Sphenolithus disbelemnos* (first occurrence [FO] at 22.41 Ma). Overgrown discoasters make it impossible to confidently identify *Discoaster druggi* (whose FO marks the base of Zone NN2 [Martini, 1971]) in the section; therefore, this sample is also assigned to combined Zone NN1/NN2. The FO of *S. disbelemnos* is identified in the following sample (8.24 m) confirms Zone NN2. This event also marks the base of Zone CNM2; however, the absence of *Triquetrorhabdulus carinatus* from the section makes it impossible to identify Zone CNM3. Therefore, this sample is assigned to combined Zone CNM2/CNM3. The crossover in abundance from *Helicosphaera euphratis* to *H. carteri* (20.89 Ma) marks the base of Zone CNM4 and is identified at 16.69 m. From 16.69 m to 43.4 m, samples are assigned to CNM4/NN2. The lowermost part of this interval contains frequent *Braarudosphaera* and *Micrantholithus*, as well as reworked Paleogene and Cretaceous (*Micula*, *Eiffellithus*) taxa. The FO of *Sphenolithus belemnos* (base of Zone CNM5, 19.01 Ma) is identified in the sample from 51.0 m. This event occurs within the lowermost part of Zone NN3. The LO of *S. belemnos* (17.96 Ma, top of Zone NN3) is identified at 68.55 m. This sample also contains the lowest identified specimen of *Helicosphaera ampliaperta*, even though the FO of this taxon is dated to 20.43 Ma (within Zone CNM4/upper NN2). It is not clear why this taxon is absent from deeper in the section as it should co-occur with *S. belemnos* throughout the latter's range. Given this, we do not use the FO of *H. ampliaperta* in the age model.

The FO of *Sphenolithus heteromorphus* (17.75 Ma, base of Zone CNM6) is found at 73.4 m. The interval between 73.4 and 96.1 m is assigned to Zone NN4 based on the co-occurrence of *S. heteromorphus* and *Helicosphaera ampliaperta*. This interval also includes the first occurrence of 6-rayed discoasters with slender rays (possibly *Discoaster exilis*); however, poor preservation precludes confident identification to the species level. Poor discoaster preservation also precludes identification of the base of Zone CNM7, which is marked by the FO of *Discoaster signus* (15.73 Ma). The LO of *Helicosphaera ampliaperta* (14.86 Ma) is found at 110.8 m, which marks the top of Zone NN4 and is within Zone CNM7. The interval between this sample and the top of the section (132.8 m) is assigned to Zone NN5/CNM7 based on the presence of *S. heteromorphus* (LO at 13.53 Ma), which is present in frequent to common numbers throughout this interval.

Age model assessment

The Backman et al. (2012) calcareous nannofossil zonation for low and middle latitudes works well for this site, which is located in the mid-latitude northern hemisphere (present day latitude = 35.1ºN). The section contains common sphenoliths and helicospheres, which dominate the marker taxa for the early to middle Miocene. Only two zonal markers could not be identified. Even though discoasters are common in the section, they are typically very overgrown, making it difficult to confidently identify taxa to species level. Therefore, we were unable to locate the FO of *Discoaster signus*, which marks the base of Zone CNM7 in the earliest middle Miocene. The absence of *Triquetrorhabdulus carinatus* also precluded identification of the base of Zone CNM3 for the early Miocene. *Triquetrorhabdulus carinatus* has been identified in other Mediterranean sections, including the Globigerina Limestone Formation in Malta (Foresi et al., 2011). However, a number of authors have noted its sporadic presence in the Mediterranean region (Foresi et al., 2014; Fornaciari and Rio, 1996; Moshkovitz and Ehrlich, 1980; Muller, 1978) making it an unreliable bioevent.

The FO of *Helicosphaera ampliaperta* (20.43 Ma) co-occurs with the LO of *Sphenolithus belemnos* (17.96 Ma) at 68.55 m. Since *S. belemnos* is present below this in the absence of *H. ampliaperta*, we do not use the FO of *H. ampliaperta* for the age model at this location, even though it has been used as a reliable bioevent in other sections around the Mediterranean. Fornaciari and Rio (1996) noted that the abundance of *H. ampliaperta* covaries with *Helicosphaera mediterranea* in Italian sections such that *H. ampliaperta* may be absent in sections where *H. mediterranea* is present. Examination of additional samples from the

Cyprus section may help to clarify if the FO of *H. ampliaperta* is unreliable or if its absence from some samples is environmental or related to the presence of other taxa.

Since we use the midpoint of the elevation between the sample in which a bioevent was identified and the next sample above (below) for last (first) occurrences (Table 2, Figures 2), this results in the LO of *S. belemnos* and the FO of *Sphenolithus heteromorphus* appearing to occur at the same stratigraphic elevation (70.98 m), even though the evolution of *S. hetermorphus* is ~200 kyr younger than the extinction of *S. belemnos*. We do not interpret this as a short hiatus, as examination of additional samples will help to more precisely locate the positions of these events. Sedimentation appears continuous and relatively constant, with a linear sedimentation rate of ~1.67 cm/kyr through the section.

Using the calcareous nannofossil biostratigraphy as a backbone, it is possible to use the carbon isotopes to further constrain the TZ section age model. The observed increase in $\delta^{13}C$ within NN4 is likely the onset of the "Monterey" carbon isotopes excursion (Vincent and Berger, 1985). This event contains well expressed $\delta^{13}C$ fluctuations that have been named $\delta^{13}C$ maximum (CM) events (Woodruff and Savin, 1991) and are now identified and tuned as long eccentricity cycles (Holbourn et al., 2007). These CM events have been previously identified in multiple sites across the Mediterranean in both bulk and benthic foraminifera carbon isotope records (Abels et al., 2005; Auer et al., 2015; Jacobs et al., 1996; John et al., 2003; Mourik et al., 2011) and are considered robust age markers. Using the nannofossils age markers to bracket the chemostratigraphy, nearly all of the CM events are identified in the record (Table 2; Figure 8).

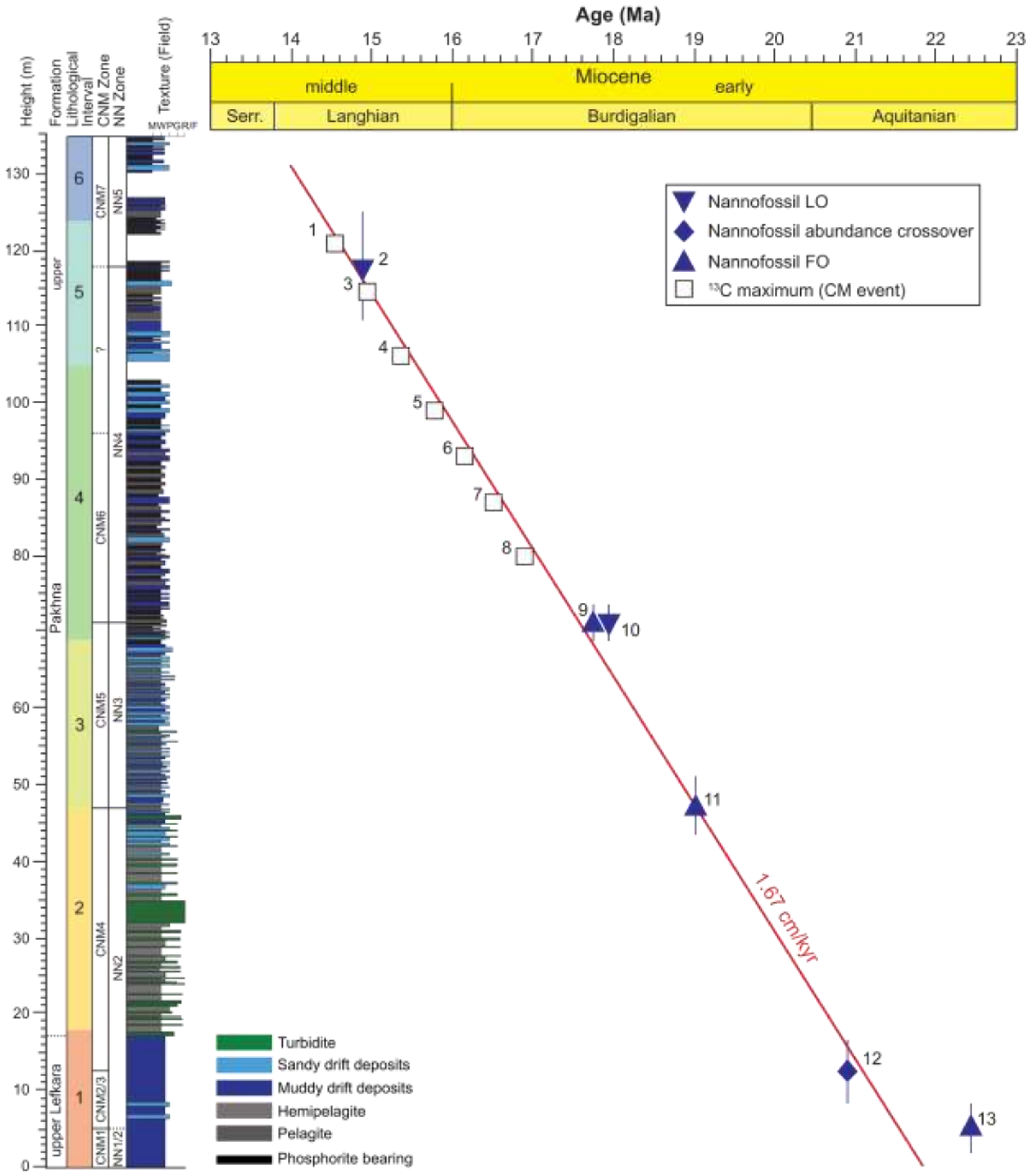

Figure 8: Age model for the TZ section based on calcareous nannofossils biostratigraphy and carbon isotope chemostratigraphy.

Discussion

Depositional history

The TZ section offers a complete and continuous depositional record of most of the lower and middle Miocene in southern Cyprus (Figure 9). The deposition in this area occurred in relatively deep water on the southern Cypriote slope and at a sedimentation rate of ~1.7cm/kyr (Figure 8). This rate appears nearly linear despite any effects from regional tectonics (Papadimitriou et al., 2018; Robertson, 1977). The lowermost part of the section (LI1) contains almost exclusively components of pelagic provenance. Upsection, the fully pelagic facies of LI1 starts to include sediment reworked from shallow water (LI2). This increase in shallower water component is also observed in the upper Oligocene to lower Miocene transition elsewhere in southern Cyprus (Hüneke et al., 2021), together with indications of bottom current activity. However, here the supply of shallow water components also indicates downslope transport, possibly due to proximity to local highs uplifted by tectonics (Papadimitriou et al., 2018). The amount of shallow-water reworked material diminishes in the next interval (LI3). Tectonic reconstructions of the region (Papadimitriou et al., 2018) infer rapid subsidence between the Burdigalian and Serravallian. This is consistent with the loss of shallow water contribution and shift to deeper water facies toward the top of the section (Figure 2). Around the mid-Burdigalian, the supply of shallow water components halts (LI4) with increased prominence of bottom current activity and increased phosphate components. This trend shifts in the Langhian (LI5) with bottom current activity diminishing in contrast with phosphate accumulation that reaches its highest levels. The resumption of bottom current activity inferred from the facies of LI6 triggered a significant decrease in phosphate content (LI6). These latter lithological intervals coinciding with local trend shifting to subsidence (Papadimitriou et al., 2018; Robertson, 1977).

Examining these trends in a larger scale perspective (Figure 10), the occurrence of shallow-water bioclast-rich intervals (LI2 and LI3) coincides with a period characterized by low global sea level (Miller et al., 2020). Similarly, the deepest part of the section based on the overwhelming dominance of planktonic foraminifera in a muddy matrix (LI5) coincides with the Miocene maximum sea level and the later resumption of bottom current activity (LI6) with a significant sea level drop. However, shallow water production in Cyprus does not resume with this sea level drop (Follows et al., 1996; Papadimitriou et al., 2018). The establishment of the shallow-water carbonate factory that supplied LI2 and LI3 occurred during the initial phase of decupling between the Indian Ocean and the Mediterranean (Bialik et al., 2019).

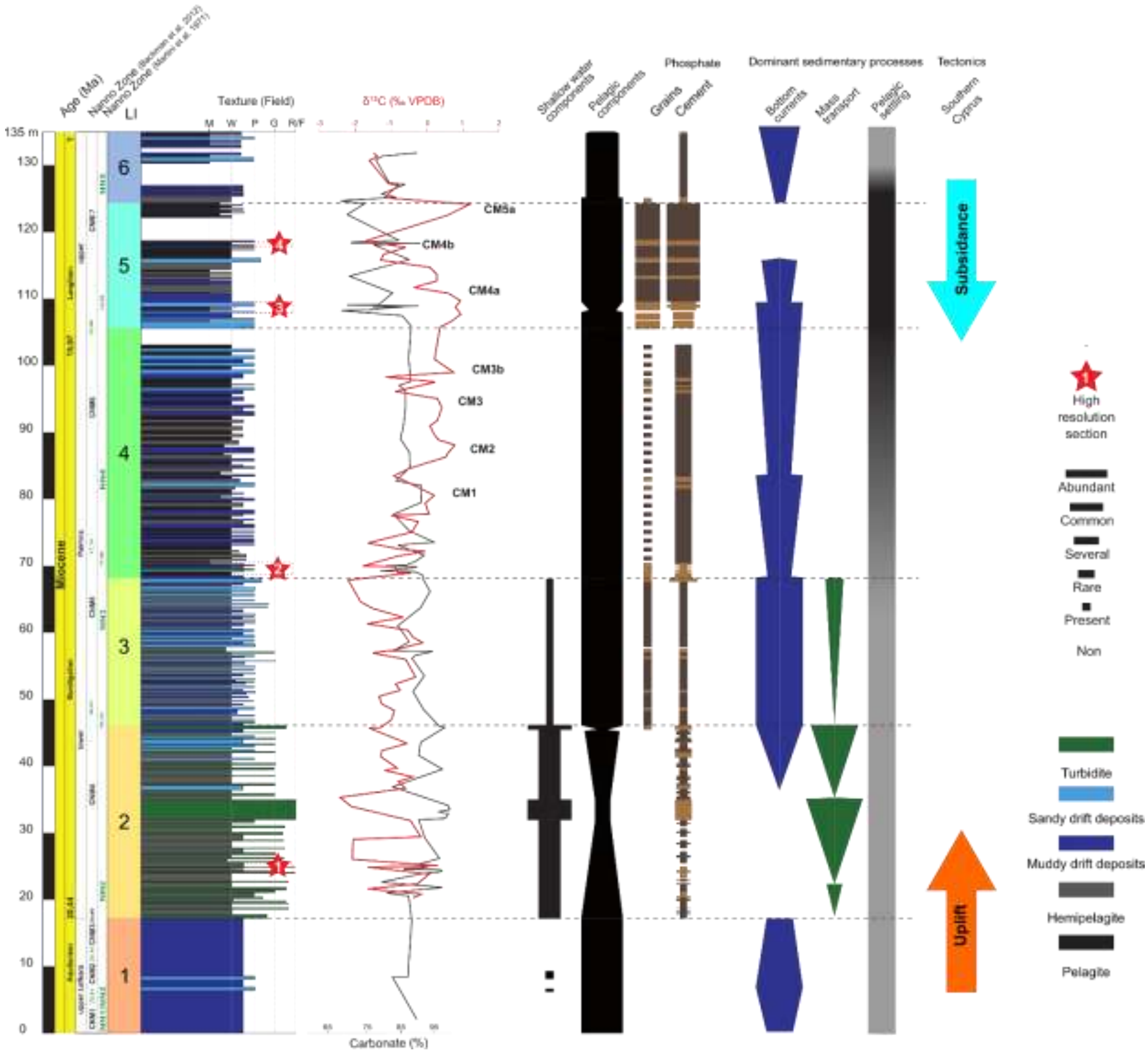

Figure 9: Synthesis of the main depositional features in the TZ section aggregating the grain component into main groups and inferred depositional conditions (bottom current influenced, mass transports and pelagic production). Local tectonic trends (Papadimitriou et al., 2018; Robertson, 1977) are noted for context.

The carbonate factory which supplied the TZ section, not preserved in the study area, constitutes the Terra Mbr. in southern Cyprus (Eaton and Robertson, 1993; Follows, 1992). The Terra Mbr. consists of different reef formations including larger flat-topped platforms and densely scattered smaller patch reefs with a rich and diverse benthic community (Coletti et al., 2021). In the late Miocene, reef building resumed in southern Cyprus, and reefs became small, linear and significantly less diverse. The termination of the

Terra Mbr. Production in the middle Miocene likely implied a combination of factors involving sea level, tectonics, and oceanographic factors. This termination predates the regional cessation of shallow-water production in the region (Buchbinder, 1996). Across the Mediterranean, reefs underwent a significant change in modes of production during the Neogene (Figure 10, Kiessling and Flügel, 2002). These shifts were ascribed to an evolutionary change of the reef builder community (Pomar et al., 2017) and shifts in nutrient supply (Halfar and Mutti, 2005). However, in the eastern Mediterranean, dramatic change in the oceanographic conditions likely also played a role and might have been the reason for apparent fewer reefs in the middle Miocene and their absence in Cyprus.

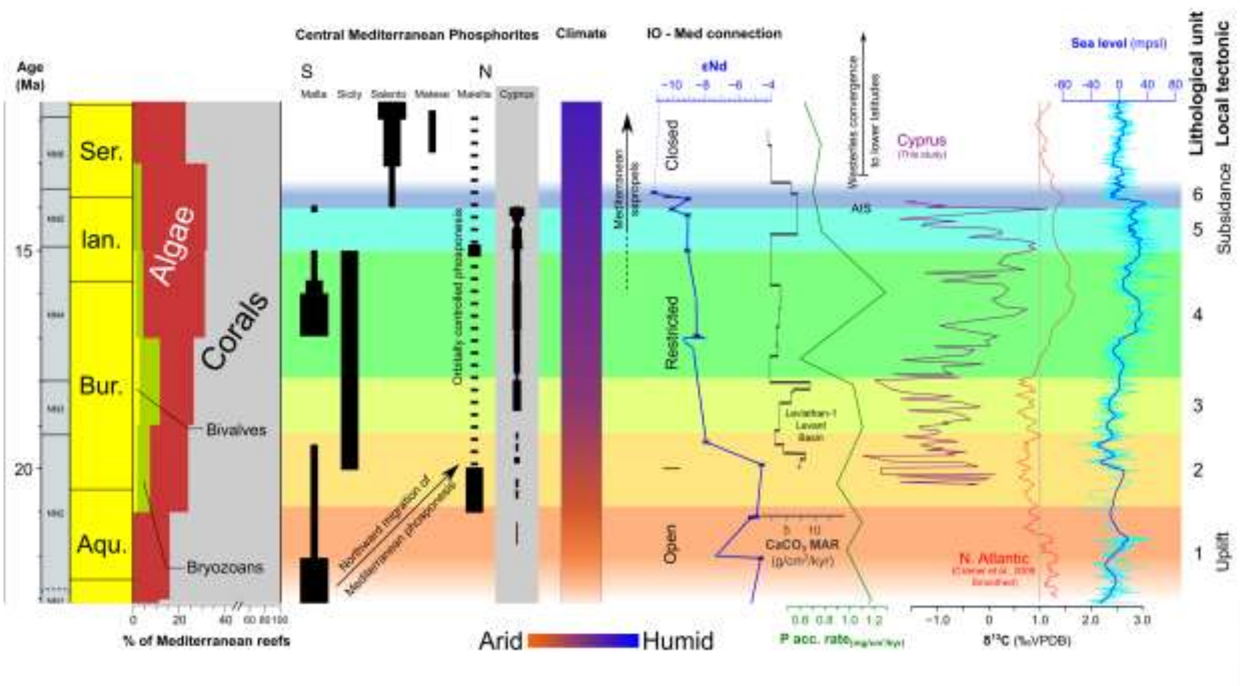

Figure 10: Regional and global context to the occurrences in the TZ section. Changes in Mediterranean reef patterns (Kiessling, 2001; Kiessling and Flügel, 2002), Mediterranean phosphate accumulation (Auer et al., 2017, 2016; Föllmi et al., 2015, 2007), regional climate patterns (Böhme et al., 2008; John et al., 2003; Schneck et al., 2010), connectivity of the Mediterranean to the Indian Ocean (IO) following (Bialik et al., 2019), initiation of sapropels (Shipboard Scientific Party, 1978; Taylforth et al., 2014), mass accumulation rate (MAR) of $CaCO_3$ in the Levant Basin (Torfstein and Steinberg, 2020), global phosphate accumulation patterns (Föllmi, 1995; Föllmi et al., 1994), high latitude climate patterns (AIS = Antarctic Ice Sheet; Flower and Kennett, 1994; Groeneveld et al., 2017), bulk rock carbon isotope record from the TZ section and benthic foraminifera carbon and oxygen isotopes from the North Atlantic (Cramer et al., 2009). Sea level curve from Miller et al. (2020).

Early to Middle evolution of the eastern Mediterranean

From the Aquitanian to Serravallian, Mediterranean oceanography and climate experienced significant rearrangements (Auer et al., 2014; Böhme et al., 2008; de la Vara and Meijer, 2016; John et al., 2003; Schneck et al., 2010). This was controlled by two main drivers: 1) the global shift of climate belts in response to high latitude (mainly Antarctic) glacial state (Flower and Kennett, 1994; Groeneveld et al., 2017); and 2) the shift in connectivity between the Mediterranean and other oceanic basins (Bialik et al., 2019; Harzhauser et al., 2007; Rögl et al., 1998; Torfstein and Steinberg, 2020). The combination of these effects resulted in the demise in productivity in the eastern Mediterranean during the latter half of the Burdigalian and the rise of sapropelic conditions (Taylforth et al., 2014; Torfstein and Steinberg, 2020). These sapropelic conditions initiated in a period of intermittent connectivity to the Indian Ocean and produced deposits dubbed "precursor sapropels" (Athanasiou et al., 2021). Such sapropelic conditions are different from those of the late Miocene and Plio-Pleistocene in intensity and frequency. In the TZ section, these are marked by reddish marl beds (notably in LI5). Similar deposits reported from northern Cyprus formed around 15.19 – 16.17 Ma, with the reddish colour ascribed to oxidised remnants of organic-rich sediments (Taylforth et al., 2014).

Phosphogenesis became prevalent in the southern central Mediterranean and parts of the northern Mediterranean during the early Miocene (Auer et al., 2016; Föllmi et al., 2007), parallel to the phosphogenesis observed in Cyprus. The Miocene phosphatisation is a departure from a long term trend where intensive phosphogenesis in the Mediterranean Tethys had, for the most part, halted as of the late Eocene (Soudry et al., 2006) due to change in circulation patterns. Phosphate accumulation later migrated primarily to the northern central Mediterranean during the middle to late Miocene (Figure 10, Föllmi *et al.*, 2015) while global phosphate accumulation rates declined (Föllmi, 1995; Föllmi et al., 1994). The global trend was attributed to changes in weathering patterns while the local Mediterranean was modulated by shifting circulation and climate patterns (Föllmi et al., 2019).

Modelling studies suggest that weakening of the anti-estuarine circulation in the Eastern Mediterranean would result in suboxic conditions bellow 500m (Stratford et al., 2000). But the impact is not uniform in deep water, with the upper part of deep waters mass more susceptible to oxygen stress due to the dynamics of intermediate water production during sapropel formation (Zirks et al., 2019). The other component of the sapropel mode is related to the rejuvenation of deep waters in the Eastern

Mediterranean, which is modulated by thermal gradients across the different sub-basins of the Eastern Mediterranean (Amitai et al., 2017). As such, a shallow sill to the Indian Ocean and a low thermal gradient from south to north would have also increased the residence time of deep water and lead to oxygen depletion. But, If the thermal gradient increased, deep and intermediate water generation would have increased too, offering an alternative mode with more active bottom currents. These alternations in bottom water circulation are clearly observed in the TZ section (LI3 onwards, notably in LI 5; Figure 8) with intervals of winnowed planktonic foraminiferal packstones (Figures 5 and 6). The transitions between varying degrees of winnowing point to intercalating levels of connectivity / influence by the world's ocean needed to invigorate circulation (de la Vara and Meijer, 2016). This activity minimized in LI5, during the final termination of connectivity to the Indian Ocean. This low activity coincides with overall salinity increase across the Mediterranean (Baldassini et al., 2021), indicating overall more significant restriction at this time. The resurgence in deepwater activity in LI6 (Figure 8) suggests the establishment of a new circulation pattern in the eastern Mediterranean, possibly due to improved connectivity to the Atlantic.

Another component to be accounted is the teleconnection to the Indian Ocean. This is to say interactions between these Mediterranean and Indian Ocean through indirect exchange (e.g. atmospheric) rather than the exchange of water that diminished ad lost across the early to middle Miocene. The initiation of cooling during the late Langhian and into the Serravallian had major impact on regional climate patterns, notably of the monsoons (Betzler et al., 2016; Bialik et al., 2020), once the Indian Ocean and the Mediterranean were fully decoupled. Today, monsoonal rainfall in east Africa is a prominent controller of the eastern Mediterranean freshwater budget through runoff of the Nile (Revel et al., 2010). The timing of initiation of the Nile as a major conduit of freshwater from east Africa to the Mediterranean is not very well constrained, but there are lines of evidence pointing to it predating the Messinian Salinity Crisis (Faccenna et al., 2019) and notably during the Langhian-Serravallian (Ouda and Obaidalla, 1995). As such, the decrease in carbonate in both the TZ section, the Levant Basin (Figure 10; Torfstein and Steinberg, 2020), and at Deep Sea Drilling Project (DSDP) Site 375 (Shipboard Scientific Party, 1978) might also indicate an increase in input of fine detritus into the eastern Mediterranean with increased monsoonal activity in east Africa. The carbonate decrease in the TZ section correlates with an increase in phosphate content.

Summary

The TZ section in southern Cyprus records a hemipelagic to pelagic carbonate-rich succession dated to the early to middle Miocene. The facies point to a deepening trend from upper to outer slope with increased winnowing of the sediment and loss of sediment transport from a shallow-water carbonate factory. The shifts in sedimentation patterns in southern Cyprus reflect both local and global changes in the environment, including the Mediterranean response to decreased water supply from the Indian Ocean and evolving thermal gradients during the early and middle Miocene. These large-scale shifts, driven by local tectonics and global climate belt shifts, set the stage for the strong circulation and freshwater balance that characterise the Mediterranean in the late Miocene and Plio-Pleistocene. Initiation of sapropels the middle Miocene is not clearly identified in this section but the preceding and coeval changes in nutrient and sedimentation pattern indicate the evolution of conditions allowing for Mediterranean sapropels.

Acknowledgements

This study was funded by the German-Israel Foundation for Scientific Research and Development (GIF) 1-1336-301.8/2016 (MioEast project) awarded to NDW and CB together with Martin Frank of GEOMAR and was carried by OMB as part of his postdoc period in University of Hamburg, there are presently supported by Marie Skłodowska Curie fellowship (101003394—RhodoMalta). DKK was funded by US National Science Foundation (NSF) grant number OCE-1326927. Additional data are available via the Figshere repository (10.6084/m9.figshare.16419771).

References

Abels, H.A., Hilgen, F.J., Krijgsman, W., Kruk, R.W., Raffi, I., Turco, E., Zachariasse, W.J., 2005. Long-period orbital control on middle Miocene global cooling: Integrated stratigraphy and astronomical tuning of the Blue Clay Formation on Malta. Paleoceanography 20, PA4012. https://doi.org/10.1029/2004PA001129

Amitai, Y., Ashkenazy, Y., Gildor, H., 2017. Multiple equilibria and overturning variability of the Aegean-Adriatic Seas. Glob. Planet. Change 151, 49–59. https://doi.org/10.1016/j.gloplacha.2016.05.004

Athanasiou, M., Triantaphyllou, M. V., Dimiza, M.D., Gogou, A., Panagiotopoulos, I., Arabas, A., Skampa, E., Kouli, K., Hatzaki, M., Tsiolakis, E., 2021. Reconstruction of oceanographic and environmental conditions in the eastern Mediterranean (Kottafi Hill section, Cyprus Island) during the middle Miocene Climate Transition. Rev. Micropaleontol. 70, 100480. https://doi.org/10.1016/j.revmic.2020.100480

Auer, G., Hauzenberger, C.A., Reuter, M., Piller, W.E., 2016. Orbitally paced phosphogenesis in Mediterranean shallow marine carbonates during the middle Miocene Monterey event. Geochemistry, Geophys. Geosystems 17, 1492–1510. https://doi.org/10.1002/2016GC006299

Auer, G., Piller, W.E., Harzhauser, M., 2014. High-resolution calcareous nannoplankton palaeoecology as a proxy for small-scale environmental changes in the Early Miocene. Mar. Micropaleontol. 111, 53–65. https://doi.org/10.1016/j.marmicro.2014.06.005

Auer, G., Piller, W.E., Reuter, M., Harzhauser, M., 2015. Correlating carbon and oxygen isotope events in early to middle Miocene shallow marine carbonates in the Mediterranean region using orbitally tuned chemostratigraphy and lithostratigraphy, Paleoceanography, 30, doi: 10.1002/2014PA002716. Received 27 AUG 2. place shallow Mar. Sect. into Glob. chronostratigraphy. Since planktonic marker species are Most. 2. https://doi.org/10.1002/2014PA002716.Received

Auer, G., Reuter, M., Hauzenberger, C.A., Piller, W.E., 2017. The impact of transport processes on rare earth element patterns in marine authigenic and biogenic phosphates. Geochim. Cosmochim. Acta 203, 140–156. https://doi.org/10.1016/j.gca.2017.01.001

Backman, J., Raffi, I., Rio, D., Fornaciari, E., Pälike, H., 2012. Biozonation and biochronology of Miocene through Pleistocene calcareous nannofossils from low and middle latitudes. Newsletters Stratigr. 45, 221–244. https://doi.org/10.1127/0078-0421/2012/0022

Bagnall, P.S., 1960. The geology and mineral resources of the Pano Lefkara-Larnaca area. Cyprus Geological Survey Department, Memoir 5.

Baldassini, N., Foresi, L.M., Lirer, F., Sprovieri, M., Turco, E., Pelosi, N., Di Stefano, A., 2021. Middle Miocene stepwise climate evolution in the Mediterranean region through high-resolution stable isotopes and calcareous plankton records. Mar. Micropaleontol. 167, 102030. https://doi.org/10.1016/j.marmicro.2021.102030

Balmer, E.M., Robertson, A.H.F., Raffi, I., Kroon, D., 2019. Pliocene–Pleistocene sedimentary development of the syntectonic Polis graben, NW Cyprus: evidence from facies analysis, nannofossil biochronology and strontium isotope dating. Geol. Mag. 156, 889–917. https://doi.org/10.1017/S0016756818000286

Betzler, C., Eberli, G.P., 2019. Miocene start of modern carbonate platforms 47, 1–5. https://doi.org/10.1130/G45994.1/4719525/g45994.pdf

Betzler, C., Eberli, G.P., Kroon, D., Wright, J.D., Swart, P.K., Nath, B.N., Alvarez-Zarikian, C.A., Alonso-García, M., Bialik, O.M., Blättler, C.L., Guo, J.A., Haffen, S., Horozal, S., Inoue, M., Jovane, L., Lanci, L., Laya, J.C., Mee, A.L.H., Lüdmann, T., Nakakuni, M., Niino, K., Petruny, L.M., Pratiwi, S.D., Reijmer, J.J.G., Reolid, J., Slagle, A.L., Sloss, C.R., Su, X., Yao, Z., Young, J.R., 2016. The abrupt onset of the modern South Asian Monsoon winds. Sci. Rep. 6, 29838. https://doi.org/10.1038/srep29838

Bialik, O.M., Auer, G., Ogawa, N.O., Kroon, D., Waldmann, N.D., Ohkouchi, N., 2020. Monsoons, Upwelling, and the Deoxygenation of the Northwestern Indian Ocean in Response to Middle to Late Miocene Global Climatic Shifts. Paleoceanogr. Paleoclimatology 35, 1–17. https://doi.org/10.1029/2019PA003762

Bialik, O.M.O.M., Frank, M., Betzler, C., Zammit, R., Waldmann, N.D.N.D., 2019. Two-step closure of the Miocene Indian Ocean Gateway to the Mediterranean. Sci. Rep. 9, 8842. https://doi.org/10.1038/s41598-019-45308-7

Blanchet, C.L., Tjallingii, R., Schleicher, A.M., Schouten, S., Frank, M., Brauer, A., 2021. Deoxygenation dynamics on the western Nile deep-sea fan during sapropel S1 from seasonal to millennial timescales. Clim. Past 17, 1025–1050. https://doi.org/10.5194/cp-17-1025-2021

Böhme, M., Ilg, A., Winklhofer, M., 2008. Late Miocene “washhouse” climate in Europe. Earth Planet. Sci. Lett. 275, 393–401. https://doi.org/10.1016/j.epsl.2008.09.011

Bosellini, F.R., Perrin, C., 2008. Estimating Mediterranean Oligocene-Miocene sea-surface temperatures: An approach based on coral taxonomic richness. Palaeogeogr. Palaeoclimatol. Palaeoecol. 258, 71–88. https://doi.org/10.1016/j.palaeo.2007.10.028

Bown, P.R., 1998. Calcareous Nannofossil Biostratigraphy, Calcareous Nannofossil Biostratigraphy. Kluwer Academie, London.

Bown, P.R., Young, J.R., 1998. Techniques, in: Bown, P.R. (Ed.), Calcareous Nannofossil Biostratigraphy. Kluwer Academie, London, pp. 16–28.

Buchbinder, B., 1996. Miocene carbonates of the eastern Mediterranean, the Red Sea and the Mesopotamian basin: geodynamic and eustatic controls. Model. Carbonate Stratigr. from Miocene Reef Complexes Mediterr. Reg. Concepts Sedimentol. Paleontol. Soc. Sediment. Geol. (SEPM)., Tulsa 5, 89–96. https://doi.org/10.2110/csp.96.01.0317

Cannings, T., Balmer, E.M., Coletti, G., Ickert, R.B., Kroon, D., Raffi, I., Robertson, A.H.F., 2021. Microfossil and strontium isotope chronology used to identify the controls of Miocene reefs and related facies in NW Cyprus. J. Geol. Soc. London. 178, jgs2020-081. https://doi.org/10.1144/jgs2020-081

Coletti, G., Balmer, E.M., Bialik, O.M., Cannings, T., Kroon, D., Robertson, A.H.F., Basso, D., 2021. Microfacies evidence for the evolution of Miocene coral-reef environments in Cyprus. Palaeogeogr. Palaeoclimatol. Palaeoecol. 110670. https://doi.org/10.1016/j.palaeo.2021.110670

Cramer, B.S., Toggweiler, J.R., Wright, J.D., Katz, M.E., Miller, K.G., 2009. Ocean overturning since the late cretaceous: Inferences from a new benthic foraminiferal isotope compilation. Paleoceanography 24, 1–14. https://doi.org/10.1029/2008PA001683

de la Vara, A., 2015. Model Analysis of the Role of Marine Gateways in the Palaeoceanography of the Miocene Mediterranean and Paratethys. Utrecht studies in Earth Sciencies, No. 98, Utrecht.

de la Vara, A., Meijer, P., 2016. Response of Mediterranean circulation to Miocene shoaling and closure of the Indian Gateway: A model study. Palaeogeogr. Palaeoclimatol. Palaeoecol. 442, 96–109. https://doi.org/10.1016/j.palaeo.2015.11.002

de la Vara, A., Meijer, P.T., Wortel, M.J.R., 2013. Model study of the circulation of the Miocene Mediterranean Sea and Paratethys: closure of the Indian Gateway. Clim. Past Discuss. 9, 4385–4424. https://doi.org/10.5194/cpd-9-4385-2013

Dunham, R.J., 1962. Classification of Carbonate Rocks According to Depositional Textures, in: Ham, W.E. (Ed.), Classification of Carbonate Rocks - A Symposium. AAPG Memoir 1, pp. 108–121.

Eaton, S., Robertson, A.H.F., 1993. The Miocene Pakhna Formation, southern Cyprus and its relationship to the Neogene tectonic evolution of the Eastern Mediterranean. Sediment. Geol. 86, 273–296.

https://doi.org/10.1016/0037-0738(93)90026-2

Faccenna, C., Glišović, P., Forte, A., Becker, T.W., Garzanti, E., Sembroni, A., Gvirtzman, Z., 2019. Role of dynamic topography in sustaining the Nile River over 30 million years. Nat. Geosci. https://doi.org/10.1038/s41561-019-0472-x

Flecker, R., Ellam, R.M.M., 2006. Identifying Late Miocene episodes of connection and isolation in the Mediterranean–Paratethyan realm using Sr isotopes. Sediment. Geol. 188–189, 189–203. https://doi.org/10.1016/j.sedgeo.2006.03.005

Flecker, R., Krijgsman, W., Capella, W., de Castro Martíns, C., Dmitrieva, E., Mayser, J.P., Marzocchi, A., Modestou, S., Ochoa, D., Simon, D., Tulbure, M., van den Berg, B., van der Schee, M., de Lange, G., Ellam, R., Govers, R., Gutjahr, M., Hilgen, F., Kouwenhoven, T., Lofi, J., Meijer, P., Sierro, F.J., Bachiri, N., Barhoun, N., Alami, A.C., Chacon, B., Flores, J.A., Gregory, J., Howard, J., Lunt, D., Ochoa, M., Pancost, R., Vincent, S., Yousfi, M.Z., 2015. Evolution of the Late Miocene Mediterranean–Atlantic gateways and their impact on regional and global environmental change. Earth-Science Rev. 150, 365–392. https://doi.org/10.1016/j.earscirev.2015.08.007

Flower, B.P., Kennett, J.P., 1994. The middle Miocene climatic transition: East Antarctic ice sheet development, deep ocean circulation and global carbon cycling. Palaeogeogr. Palaeoclimatol. Palaeoecol. 108, 537–555. https://doi.org/10.1016/0031-0182(94)90251-8

Föllmi, K.B., 1995. 160 m.y. record of marine sedimentary phosphoeus burial: Coupling of climte and continental weathering under greenhouse and icehous conditions. Geology 23, 859–862.

Föllmi, K.B., Gertsch, B., Renevey, J.-P., De Kaenel, E., Stille, P., 2007. Stratigraphy and sedimentology of phosphate-rich sediments in Malta and south-eastern Sicily (latest Oligocene to early Late Miocene). Sedimentology 55, 1029–1051. https://doi.org/10.1111/j.1365-3091.2007.00935.x

Föllmi, K.B., Hofmann, H., Chiaradia, M., de Kaenel, E., Frijia, G., Parente, M., 2015. Miocene phosphate-rich sediments in Salento (southern Italy). Sediment. Geol. 327, 55–71. https://doi.org/10.1016/j.sedgeo.2015.07.009

Föllmi, K.B., Schöllhorn, I., Ulianov, A., Adatte, T., Spangenberg, J.E., de Kaenel, E., Gertsch, B., Schwennicke, T., Ledesma, M.C., Grimm, K.A., Garrison, R.E., 2019. Phosphogenesis during the Cenozoic transition from greenhouse to icehouse conditions: Upper Oligocene to lower Miocene siliceous, phosphate, and organic-rich sediments near La Purísima, Baja California Sur, Mexico.

Depos. Rec. 5, 23–52. https://doi.org/10.1002/dep2.52

Föllmi, K.B., Weissert, H., Bisping, M., Funk, H., 1994. Phosphogenesis, carbon-isotope stratigraphy, and carbonate-platform evolution along the Lower Cretaceous northern Tethyan margin. Geol. Soc. Am. Bull. 106, 729–746.

Follows, E.J., 1992. Patterns of reef sedimentation and diagenesis in the Miocene of Cyprus. Sediment. Geol. 79, 225–253. https://doi.org/10.1016/0037-0738(92)90013-H

Follows, E.J., Robertson, A.H.F., Scoffin, T.P., 1996. Tectonic controls on Miocene reefs and related carbonate facies in Cyprus, in: Franseen, E.K., Esteban, M., Ward, W.C., Rouchy, J.-M. (Eds.), Models for Carbonate Stratigraphy from Miocene Reef Complexes of Mediterranean Regions. SEPM Concepts in Sedimentology and Paleontology 5, pp. 295–315. https://doi.org/10.2110/csp.96.01.0295

Foresi, L.M., Baldassini, N., Sagnotti, L., Lirer, F., Di Stefano, A., Caricchi, C., Verducci, M., Salvatorini, G., Mazzei, R., 2014. Integrated stratigraphy of the St. Thomas section (Malta Island): A reference section for the lower Burdigalian of the Mediterranean Region. Mar. Micropaleontol. 111, 66–89. https://doi.org/10.1016/j.marmicro.2014.06.004

Foresi, L.M., Verducci, M., Baldassini, N., Lirer, F., Mazzei, R., Gianfranco, S., Ferraro, L., Da Prato, S., 2011. Integrated stratigraphy of St. Peter's Pool section (Malta): new age for the Upper Globigerina Limestone member and progress towards the Langhian GSSP. Stratigraphy 8, 125–143.

Fornaciari, E., Rio, D., 1996. Latest Oligocene to early middle Miocene quantitative calcareous nannofossil biostratigraphy in the Mediterranian region. Micropaleontology 42, 1–36.

Geological survey department, 1979. Geological map of Cyprus 1:250,000. Lefkosia.

Griffin, D.L., 2002. Aridity and humidity: Two aspects of the late Miocene climate of North Africa and the Mediterranean. Palaeogeogr. Palaeoclimatol. Palaeoecol. 182, 65–91. https://doi.org/10.1016/S0031-0182(01)00453-9

Groeneveld, J., Henderiks, J., Renema, W., McHugh, C.M., De Vleeschouwer, D., Christensen, B.A., Fulthorpe, C.S., Reuning, L., Gallagher, S.J., Bogus, K., Auer, G., Ishiwa, T., 2017. Australian shelf sediments reveal shifts in Miocene Southern Hemisphere westerlies. Sci. Adv. 3, e1602567. https://doi.org/10.1126/sciadv.1602567

Halfar, J., Mutti, M., 2005. Global dominance of coralline red-algal facies: A response to Miocene oceanographic events. Geology 33, 481–484. https://doi.org/10.1130/G21462.1

Hamon, N., Sepulchre, P., Lefebvre, V., Ramstein, G., 2013. The role of eastern tethys seaway closure in the middle miocene climatic transition (ca. 14 Ma). Clim. Past 9, 2687–2702. https://doi.org/10.5194/cp-9-2687-2013

Harzhauser, M., Kroh, A., Mandic, O., Piller, W.E., Göhlich, U., Reuter, M., Berning, B., 2007. Biogeographic responses to geodynamics: A key study all around the Oligo–Miocene Tethyan Seaway. Zool. Anzeiger - A J. Comp. Zool. 246, 241–256. https://doi.org/10.1016/j.jcz.2007.05.001

Holbourn, A., Kuhnt, W., Schulz, M., Flores, J.-A.A., Andersen, N., 2007. Orbitally-paced climate evolution during the middle Miocene “Monterey” carbon-isotope excursion. Earth Planet. Sci. Lett. 261, 534–550. https://doi.org/10.1016/j.epsl.2007.07.026

Hüneke, H., Hernández-Molina, F.J., Rodríguez-Tovar, F.J., Llave, E., Chiarella, D., Mena, A., Stow, D.A.V., 2021. Diagnostic criteria using microfacies for calcareous contourites, turbidites and pelagites in the Eocene–Miocene slope succession, southern Cyprus. Sedimentology 68, 557–592. https://doi.org/10.1111/sed.12792

Jacobs, E., Weissert, H., Shields, G., Stille, P., 1996. The Monterey Event in the Mediterranean: A record from shelf sediments of Malta. Paleoceanography 11, 717–728. https://doi.org/10.1029/96PA02230

John, C.M., Mutti, M., Adatte, T., 2003. Mixed carbonate-siliciclastic record on the North African margin (Malta) - Coupling of weathering processes and mid Miocene climate. Bull. Geol. Soc. Am. 115, 217–229. https://doi.org/10.1130/0016-7606(2003)115<0217:MCSROT>2.0.CO;2

Kähler, G., Stow, D.A.V., 1998. Turbidites and contourites of the Palaeogene Lefkara Formation, southern Cyprus. Sediment. Geol. 115, 215–231. https://doi.org/10.1016/S0037-0738(97)00094-8

Kiessling, W., 2001. Phanerozoic reef trends based on the Paleoreef database, in: Stanley, G.D.J. (Ed.), The History and Sedimentology of Ancient Reef Systems. Springer, Boston, MA, pp. 41–88. https://doi.org/10.1007/978-1-4615-1219-6_2

Kiessling, W., Flügel, E., 2002. PALEOREEFS—a database on Phanerozoic reefs, in: Kiessling, W., Flügel, E., Golonka, J. (Eds.), Phanerozoic Reef Patterns. SEPM (Society for Sedimentary Geology), pp. 77–

92. https://doi.org/10.2110/pec.02.72.0077

Kroon, D., Alexander, I., Little, M., Lourens, L.J., Matthewson, A., Robertson, A.H.F., Sakamoto, T., 2004. Oxygen isotope and sapropel stratigraphy in the Eastern Mediterranean during the last 3.2 million years 160, 181–189.

Larrasoaña, J.C., Roberts, A.P., Rohling, E.J., Winklhofer, M., Wehausen, R., 2003. Three million years of monsoon variability over the northern Sahara. Clim. Dyn. 21, 689–698. https://doi.org/10.1007/s00382-003-0355-z

Magazzù, G., Decembrini, F., 1995. Primary production, biomass and abundance of phototrophic picoplankton in the Mediterranean Sea: a review. Aquat. Microb. Ecol. 9, 97–104. https://doi.org/10.3354/ame009097

Martini, E., 1971. Standard Tertiary and Quaternary calcareous nannoplankton zonation, in: Farinacci A. (Ed.), Proceedings of the Second Planktonic Conference, Vol. II. Roma, Tecnoscienza, Rome, pp. 739–785.

Meilijson, A., Hilgen, F., Sepúlveda, J., Steinberg, J., Fairbank, V., Flecker, R., Waldmann, N.D., Spaulding, S.A., Bialik, O.M., Boudinot, F.G., Illner, P., Makovsky, Y., 2019. Chronology with a pinch of salt: Integrated stratigraphy of Messinian evaporites in the deep Eastern Mediterranean reveals long-lasting halite deposition during Atlantic connectivity. Earth-Science Rev. 194, 374–398. https://doi.org/10.1016/j.earscirev.2019.05.011

Miguez-Salas, O., Rodríguez-Tovar, F.J., 2019. Ichnofacies distribution in the Eocene-Early Miocene Petra Tou Romiou outcrop, Cyprus: sea level dynamics and palaeoenvironmental implications in a contourite environment. Int. J. Earth Sci. 108, 2531–2544. https://doi.org/10.1007/s00531-019-01775-x

Miller, K.G., Browning, J. V., Schmelz, W.J., Kopp, R.E., Mountain, G.S., Wright, J.D., 2020. Cenozoic sea-level and cryospheric evolution from deep-sea geochemical and continental margin records. Sci. Adv. 6, eaaz1346. https://doi.org/10.1126/sciadv.aaz1346

Miller, K.G., Wright, J.D., Fairbanks, R.G., 1991. Unlocking the Ice House: Oligocene-Miocene oxygen isotopes, eustasy, and margin erosion. J. Geophys. Res. Solid Earth 96, 6829–6848. https://doi.org/10.1029/90JB02015

Moshkovitz, S., Ehrlich, A., 1980. Distribution of the calcareous nannofossils in the Neogene sequence of Jaffa-1 Borehole, Central Coastal Plain, Israel. Jerusalem.

Mourik, A.A., Abels, H.A., Hilgen, F.J., Di Stefano, A., Zachariasse, W.J., 2011. Improved astronomical age constraints for the middle Miocene climate transition based on high-resolution stable isotope records from the central Mediterranean Maltese Islands. Paleoceanography 26, PA1210. https://doi.org/10.1029/2010PA001981

Muller, C., 1978. Neogene calcareous nannofossils from the Meditreranean Leg 42A of the DSDP, in: Hsü, K.J., Montadert, L. (Eds.), Initial Reports of the Deep Sea Drilling Project, 42 Pt. 1. U.S. Government Printing Office, pp. 727–751. https://doi.org/10.2973/dsdp.proc.42-1.132.1978

Ouda, K.H., Obaidalla, N., 1995. The Geologic Evolution of the Nile Delta Area During the Oligocene-Miocene. Egypt. J. Geol.

Papadimitriou, N., Deschamps, R., Symeou, V., Souque, C., Gorini, C., Nader, F.H., Blanpied, C., 2018. The tectonostratigraphic evolution of Cenozoic basins of the Northern Tethys: The Northern margin of the Levant Basin. Oil Gas Sci. Technol. 73, 77. https://doi.org/10.2516/ogst/2018085

Perch-Nielsen, K., 1985. Mesozoic calcareous nannofossils, in: Bolli, H.M., Saunders, J.B., Perch-Nielsen, K. (Eds.), Plankton Stratigraphy. Cambridge University Press, Cambridge, pp. 329–426.

Pomar, L., Baceta, J.I., Hallock, P., Mateu-Vicens, G., Basso, D., 2017. Reef building and carbonate production modes in the west-central Tethys during the Cenozoic. Mar. Pet. Geol. 83, 261–304. https://doi.org/10.1016/j.marpetgeo.2017.03.015

Pomar, L., Hallock, P., 2007. Changes in coral-reef structure through the Miocene in the Mediterranean province: Adaptive versus environmental influence. Geology 35, 899–902. https://doi.org/10.1130/G24034A.1

Pound, M.J., Haywood, A.M., Salzmann, U., Riding, J.B., 2012. Global vegetation dynamics and latitudinal temperature gradients during the Mid to Late Miocene (15.97-5.33Ma). Earth-Science Rev. 112, 1–22. https://doi.org/10.1016/j.earscirev.2012.02.005

Reich, T., Ben-Ezra, T., Belkin, N., Tsemel, A., Aharonovich, D., Roth-Rosenberg, D., Givati, S., Bialik, O., Herut, B., Berman-Frank, I., Frada, M., Krom, M.D., Lehahn, Y., Rahav, E., Daniel Sher, 2021. Seasonal dynamics of phytoplankton and bacterioplankton at the ultra-oligotrophic southeastern

Mediterranean Sea. bioRxiv. https://doi.org/10.1101/2021.03.24.436734

Reolid, J., Betzler, C., Bialik, O.M., Waldman, N., 2020. Lenticular-bedding-like bioturbation and the onshore recognition of carbonate drifts (Oligocene, Cyprus). J. Sediment. Res. 90, 1667–1677. https://doi.org/10.2110/jsr.2020.70

Reuter, M., Piller, W.E., Brandano, M., Harzhauser, M., 2013. Correlating Mediterranean shallow water deposits with global Oligocene-Miocene stratigraphy and oceanic events. Glob. Planet. Change 111, 226–236. https://doi.org/10.1016/j.gloplacha.2013.09.018

Revel, M., Ducassou, E., Grousset, F.E., Bernasconi, S.M., Migeon, S., Revillon, S., Mascle, J., Murat, a., Zaragosi, S., Bosch, D., 2010. 100,000 Years of African monsoon variability recorded in sediments of the Nile margin. Quat. Sci. Rev. 29, 1342–1362. https://doi.org/10.1016/j.quascirev.2010.02.006

Robertson, A.H.F., 1977. Tertiary uplift history of the Troodos massif, Cyprus. Bull. Geol. Soc. Am. 88, 1763–1772. https://doi.org/10.1130/0016-7606(1977)88<1763:TUHOTT>2.0.CO;2

Robertson, A.H.F., 1976. Pelagic Chalks and Calciturbidites from the Lower Tertiary of the Troodos Massif, Cyprus. J. Sediment. Res. 46, 1007–1016. https://doi.org/10.1306/212F70BD-2B24-11D7-8648000102C1865D

Robertson, A.H.F., Hudson, J.D., 2009. Pelagic Sediments in the Cretaceous and Tertiary History of the Troodos Massif, Cyprus, in: Hsü, K.J., Jenkyns, H.C. (Eds.), Pelagic Sediments: On Land and under the Sea. Blackwell Publishing Ltd., Oxford, UK, pp. 403–436. https://doi.org/10.1002/9781444304855.ch19

Robinson, A.R., Malanotte-Rizzoli, P., Hecht, A., Michelato, A., Roether, W., Theocharis, A., Ünlüata, Ü., Pinardi, N., Artegiani, A., Bergamasco, A., Bishop, J., Brenner, S., Christianidis, S., Gacic, M., Georgopoulos, D., Golnaraghi, M., Hausmann, M., Junghaus, H.-G., Lascaratos, A., Latif, M.A., Leslie, W.G., Lozano, C.J., Og˛uz, T., Özsoy, E., Papageorgiou, E., Paschini, E., Rozentroub, Z., Sansone, E., Scarazzato, P., Schlitzer, R., Spezie, G.-C., Tziperman, E., Zodiatis, G., Athanassiadou, L., Gerges, M., Osman, M., 1992. General circulation of the Eastern Mediterranean. Earth-Science Rev. 32, 285–309. https://doi.org/10.1016/0012-8252(92)90002-B

Rodríguez-Tovar, F.J., Hernández-Molina, F.J., Hüneke, H., Llave, E., Stow, D., 2019. Contourite facies model: Improving contourite characterization based on the ichnological analysis. Sediment. Geol. 384, 60–69. https://doi.org/10.1016/j.sedgeo.2019.03.010

Rögl, V.F., Rögl, F., Rögl, V.F., 1998. Palaeogeographic Considerations for Mediterranean and Paratethys Seaways (Oligocene to Miocene). Ann. des Naturhistorischen Museums Wien 99A, 279–310.

Rohling, E.J., Marino, G., Grant, K.M., 2015. Mediterranean climate and oceanography, and the periodic development of anoxic events (sapropels). Earth-Science Rev. 143, 62–97. https://doi.org/10.1016/j.earscirev.2015.01.008

Sant, K., V. Palcu, D., Mandic, O., Krijgsman, W., 2017. Changing seas in the Early–Middle Miocene of Central Europe: a Mediterranean approach to Paratethyan stratigraphy. Terra Nov. 29, 273–281. https://doi.org/10.1111/ter.12273

Schneck, R., Micheels, A., Mosbrugger, V., 2010. Climate modelling sensitivity experiments for the Messinian Salinity Crisis. Palaeogeogr. Palaeoclimatol. Palaeoecol. 286, 149–163. https://doi.org/10.1016/j.palaeo.2009.12.011

Seidenkrantz, M.-S., Kouwenhoven, T.., Jorissen, F.., Shackleton, N.., van der Zwaan, G.., 2000. Benthic foraminifera as indicators of changing Mediterranean–Atlantic water exchange in the late Miocene. Mar. Geol. 163, 387–407. https://doi.org/10.1016/S0025-3227(99)00116-4

Shaanan, U., Avigad, D., Morag, N., Güngör, T., Gerdes, A., 2021. Drainage response to Arabia–Eurasia collision: Insights from provenance examination of the Cyprian Kythrea flysch (Eastern Mediterranean Basin). Basin Res. 33, 26–47. https://doi.org/10.1111/bre.12452

Shipboard Scientific Party, 1978. Sites 375 and 376: Florence Rise, in: Hsü, K.J., Montadert, L. (Eds.), Initial Reports of the Deep Sea Drilling Project, 42 Pt. 1. U.S. Government Print Office, College Station, Texas, pp. 219–304. https://doi.org/10.2973/dsdp.proc.42-1.106.1978

Simon, D., Palcu, D., Meijer, P., Krijgsman, W., 2018. The sensitivity of middle Miocene paleoenvironments to changing marine gateways in Central Europe. Geology. https://doi.org/10.1130/G45698.1

Soudry, D., Glenn, C.R., Nathan, Y., Segal, I., VonderHaar, D., 2006. Evolution of Tethyan phosphogenesis along the northern edges of the Arabian-African shield during the Cretaceous-Eocene as deduced from temporal variations of Ca and Nd isotopes and rates of P accumulation. Earth-Science Rev. 78, 27–57.

Stow, D.A. V., Kahler, G., Reeder, M., 2002. Fossil contourites: type example from an Oligocene palaeoslope system, Cyprus, in: Stow, D.A.V., Pudsey, C.J., Howe, J.A., Faugères, J.C., Viana, A.R. (Eds.), Deep-Water Contourite Systems: Modern Drifts and Ancient Series, Seismic and Sedimentary Characteristics. Geological Society, London, Memoirs 22, pp. 443–455. https://doi.org/10.1144/GSL.MEM.2002.022.01.31

Stratford, K., Williams, R.G., Myers, P.G., 2000. Impact of the circulation on Sapropel Formation in the eastern Mediterranean. Global Biogeochem. Cycles 14, 683–695. https://doi.org/10.1029/1999GB001157

Swezey, C.S., 2009. Cenozoic stratigraphy of the Sahara, Northern Africa. J. African Earth Sci. 53, 89–121. https://doi.org/10.1016/j.jafrearsci.2008.08.001

Taylforth, J.E., McCay, G.A., Ellam, R., Raffi, I., Kroon, D., Robertson, A.H.F., 2014. Middle Miocene (Langhian) sapropel formation in the easternmost Mediterranean deep-water basin: Evidence from northern Cyprus. Mar. Pet. Geol. 57, 521–536. https://doi.org/10.1016/j.marpetgeo.2014.04.015

Torfstein, A., Steinberg, J., 2020. The Oligo–Miocene closure of the Tethys Ocean and evolution of the proto-Mediterranean Sea. Sci. Rep. 10, 1–10. https://doi.org/10.1038/s41598-020-70652-4

Vincent, E., Berger, W.H., 1985. Carbon dioxide and polar cooling in the Miocene: The Monterey hypothesis, in: Sundquist, E.T., Broecker, W.S. (Eds.), The Carbon Cycle and Atmospheric CO: Natural Variations Archean to Present. Washington, D.C., pp. 455–468. https://doi.org/10.1029/GM032p0455

Woodruff, F., Savin, S., 1991. Mid-Miocene isotope stratigraphy in the deep sea: High-resolution correlations, paleoclimatic cycles, and sediment preservation. Paleoceanography 6, 755–806. https://doi.org/10.1029/91PA02561

Young, J.R., Bown, P.R., A., L.J., 2019. Nannotax3 [WWW Document]. Int. Nannoplankt. Assoc.

Zhang, Z., Ramstein, G., Schuster, M., Li, C., Contoux, C., Yan, Q., 2014. Aridification of the Sahara desert caused by Tethys Sea shrinkage during the Late Miocene. Nature 513, 401–4. https://doi.org/10.1038/nature13705

Zirks, E., Krom, M., Schmiedl, G., Katz, T., Xiong, Y., Alcott, L.J., Poulton, S.W., Goodman-Tchernov, B., 2021. Redox evolution and the development of oxygen minimum zones in the Eastern Mediterranean Levantine basin during the early Holocene. Geochim. Cosmochim. Acta 297, 82–

100. https://doi.org/10.1016/j.gca.2021.01.009

Zirks, E., Krom, M.D., Zhu, D., Schmiedl, G., Goodman-Tchernov, B.N., 2019. Evidence for the Presence of Oxygen-Depleted Sapropel Intermediate Water across the Eastern Mediterranean during Sapropel S1. ACS Earth Sp. Chem. 3, 2287–2297. https://doi.org/10.1021/acsearthspacechem.9b00128

Tables

Name	Grain size, sorting, and texture	Major components	Minor Components	Preservation of the components	Matrix/Cement	Sedimentary structures
Mass transport deposits	Poor- to medium-sorted, silt- to pebble-sized packstone to floatstone/rudstone.	LBF, red algae, unidentifiable bioclasts, and planktonic foraminífera.	Benthic foraminifera, mollusks fragments, echinoids, bryozoan, fish debris (phosphate grains), coral fragments, lithoclasts, siliciclastics.	Fragmentation is abundant. Fragments of the larger bioclasts (i.e, corals, mollusks…) and lithoclasts are angular, and unidentifiable bioclasts are mostly rounded.	Micrite and locally microgranular. Locally phasphatic cements.	None sedimentary structures observed.
Sandy drift deposits	Well-sorted, fine grained packstone.	Planktonic foraminifera.	Unidentifiable bioclasts, benthic foraminifera, mollusks, red algae, LBF, and equinoid fragments. Fish debris (phosphate grains).	Planktonic foraminifera may be fragmented. Mollusks, equinoids, red algae, and LBF are fragmented.	Micrite, rarely microgranular (planktonic foraminifera fragments).	Intensely bioturbated. Locally wavy and parallel lamination.
Muddy drift deposits	Well-sorted, silt to fine grained packstone.	Planktonic foraminifera.	Unidentifiable bioclasts and benthic foraminifera. Fish debris (phosphate grains). Rare siliciclastic grains.	Planktonic foraminifera may be fragmented.	Micrite.	Intensely bioturbated. *Zoophycos* burrows may mimic lenticular bedding. Locally wavy and parallel lamination.
Hemipelagite	Medium-sorted, mud-rich wackestone to packstone.	Unidentifiable silt-sized bioclasts and planktonic foraminifera.	Benthic foraminifera. Fish debris (phosphate grains). Rare siliciclastic grains.	Rare fragmentation of the planktonic foraminifera.	Micrite. Locally phosphatic cements.	Intensely bioturbated. None sedimentary structures observed.
Pelagite	Medium-sorted, mud-rich mudstone to wackestone.	Planktonic foraminifera.	Fish debris, benthic foraminifera, unidentifiable bioclast and rare siliciclastics.	Rare fragmentation of the bioclasts.	Micrite. Abundant phosphatic cement.	Intensely bioturbated. Rarely fine horizontal parallel lamination.

Table 1: Sedimentary components and environmental interpretation of the different facies in the TZ section.

Datum Label	Height in section (m)			Marker	Event	Age (Ma)	References
	Event identified	Next sample above/below	Midpoint				
	132.8 (top of section)			LO *Sphenolithus heteromorphus* (not observed)	Base NN6	>13.53	Martini, 1971; Backman et al., 2012
1	121			First well defined $\delta^{13}C$ peak above base of NN5	CM5a	14.55	Holbourn et al., 2007
2	110.8	125.1	117.95	LO *Helicosphaera ampliaperta*	Base NN5	14.86	Martini, 1971; Backman et al., 2012
3	114.5			Sixth well defined $\delta^{13}C$ peak above base of NN4 following CM3b	CM4b	14.95	Holbourn et al., 2007
4	106			Fifth well defined $\delta^{13}C$ peak above base of NN4 following CM3a	CM4a	15.38	Holbourn et al., 2007
5	99			Fourth well defined $\delta^{13}C$ peak above base of NN4 following CM3a	CM3b	15.78	Holbourn et al., 2007
6	93			Third well defined $\delta^{13}C$ peak above base of NN4 following CM2	CM3a	16.15	Holbourn et al., 2007
7	87			Second well defined $\delta^{13}C$ peak above base of NN4 following CM1	CM2	16.52	Holbourn et al., 2007
8	80			First well defined $\delta^{13}C$ peak above base of NN4	CM1	16.9	Holbourn et al., 2007
9	73.4	68.55	70.98	FO *Sphenolithus heteromorphus*	Base CNM6	17.75	Backman et al., 2012
10	68.55	73.4	70.98	LO *Sphenolithus belemnos*	Base NN4	17.96	Martini, 1971; Backman et al., 2012
11	51.0	43.4	47.2	FO *Sphenolithus belemnos*	Base CNM5	19.01	Backman et al., 2012
12	16.69	8.24	12.47	X *Helicosphaera euphratis / H. carteri*	Base CNM4	20.89	Backman et al., 2012
13	8.24	1.94	5.09	FO *Sphenolithus disbelemnos*	Base CNM2	22.41	Backman et al., 2012
	1.94 (base of section)			LO Sphenolithus delphix (not observed)	Base CNM1	<23.06	Backman et al., 2012

Table 2: Biostratigraphic and chemostratigraphic datums used for the TZ section age model.